Research Article Vol. 29, No. 2 / 18 January 2021 / Optics Express 1221
Optics EXPRESS

Characterization of deep sub-wavelength nanowells by imaging the photon state scattering spectra

WEIPING LIU,[1,7] JICHUAN XIONG,[1,7] LIBO ZHU,[2] SHENGWEI YE,[3] HANWEN ZHAO,[1] JUAN LIU,[1] HENG ZHANG,[1] LIANPING HOU,[3] JOHN H. MARSH,[3] LEI DONG,[4] XIAOHONG W. GAO,[5] DAMING SHI,[6] AND XUEFENG LIU[1,*]

[1]*School of Electronic and Optical Engineering, Nanjing University of Science and Technology, Nanjing 210094, China*
[2]*School of Biological Science and Medical Engineering, Southeast University, Nanjing, 210096, China*
[3]*James Watt School of Engineering, University of Glasgow, Glasgow, G12 8QQ, UK*
[4]*School of Life Science, Beijing Institute of Technology, Beijing, China*
[5]*Department of Computer Science, Middlesex University, London NW4 4BT, UK*
[6]*College of Computer Science and Software Engineering, Shenzhen University, China*
[7]*W. Liu. and J. Xiong. contributed equally to the manuscript*
[*]*liuxf_1956@sina.com*

Abstract: Optical-matter interactions and photon scattering in a sub-wavelength space are of great interest in many applications, such as nanopore-based gene sequencing and molecule characterization. Previous studies show that spatial distribution features of the scattering photon states are highly sensitive to the dielectric and structural properties of the nanopore array and matter contained on or within them, as a result of the complex optical-matter interaction in a confined system. In this paper, we report a method for shape characterization of subwavelength nanowells using photon state spatial distribution spectra in the scattering near field. Far-field parametric images of the near-field optical scattering from sub-wavelength nanowell arrays on a SiN substrate were obtained experimentally. Finite-difference time-domain simulations were used to interpret the experimental results. The rich features of the parametric images originating from the interaction of the photons and the nanowells were analyzed to recover the size of the nanowells. Experiments on nanoholes modified with Shp2 proteins were also performed. Results show that the scattering distribution of modified nanoholes exhibits significant differences compared to empty nanoholes. This work highlights the potential of utilizing the photon status scattering of nanowells for molecular characterization or other virus detection applications.

1. Introduction

Analytical systems using scattering of light from solid-state nanopores are attractive in molecular sensing applications because of their high sensitivity, versatility in detecting different kinds of molecules and potential for integration in compact and miniature systems. Until recently, solid-state nanopores have been mainly used as molecule biosensors by detecting changes in the electrical ion current when molecules in an ionic solution are translocated through the nanopores under the influence of an electric current. This kind of measurement has been utilized in many applications including single-molecule nucleic acid sequencing [1–9], probing of RNA structures [6,10–12], and proteins [13–15], genotyping of viral genes [16,17], and even distinguishing fine macromolecular properties [18].

However, solid-state nanopore systems face challenges in many commercial applications in terms of their measurement noise, bandwidth, throughput, and spatial resolution. Although there

#413942 https://doi.org/10.1364/OE.413942
Journal © 2021 Received 5 Nov 2020; revised 12 Dec 2020; accepted 14 Dec 2020; published 6 Jan 2021

Optics EXPRESS

have been efforts to improve the electrical ion measurement approach [19–23], many studies have begun to employ optical detection to complement or as an alternative to electrical detection [24–28]. While electrical sensing relies on electron flow due to the translocation of the molecule through the nanopore, optical sensing can be performed in the far-field. Optical systems can access a wider range of reagents, and make use of high sensitivity photon sensors including Avalanche Photo Diodes (APDs), Electron-Multiplying CCD and scientific CMOS imagers, together with solid-state light sources covering the spectrum from the near UV to the IR. Most importantly, optical sensing techniques open opportunities for high throughput parallel sensing by employing a nanopore array and wide-field imaging system.

In previous optically-based methods, light scattered from the nanopore and its vicinity is one of the major sources of background noise, especially when detecting individual fluorophores in single-molecule sensing applications. Total Internal Reflection Fluorescence (TIRF) [24–26] and confocal illumination [27,28] have been used to suppress the background light. Modifications of the surface of the nanopore have also been introduced to minimize the scattered background light noise [29]. It has been recently shown that ultra-high Q resonances can be realized in metallic structures for extreme imaging applications [30,31]. These methods either require sophisticated optical configurations or complex processing of the nanostructures. Scanning near-field optical microscopy (SNOM) has also been widely used in various nanoscopic applications to provide a better understanding of the interactions between objects and fields at the nanometric scale [32]. Techniques include aperture SNOM [33], apertureless (scattering) SNOM [34], and variations such as photon scanning tunneling microscopy (PSTM) [35]. Although high spatial resolution can be achieved using SNOM, the imaging speed and efficiency cannot meet the requirements for high throughput sensing of molecules, but these requirements are achievable using wide-field optical imaging of a nanopore array.

In this paper, we propose the utilization of a simple and robust Polarization parametric Indirect Microscopic Imaging (PIMI) method for optical characterization of nanopores. As a proof of concept, a nanowell array was fabricated to demonstrate the principle of the method. A wide-field imaging system was implemented, and photon status spatial distribution spectra were measured which reflect the shape characteristics of the nanowell. Unlike Conventional Microscopes (CM), whose resolution is limited by the Abbe diffraction limit, sub-wavelength morphologic information about the nanowell can be retrieved from the photon status distributions in the PIMI method. Instead of making efforts to suppress the background noise resulting from the light scattered by the nanowell and its vicinity, this approach recovers information about the nanowell directly from the scattering electric field around the nanowell. In single-molecule sensing applications, the photon status distributions will contain not only information about the nanowell but also information about the molecule translocating through or captured in the nanowell. This makes the method useful for single molecule sensing applications.

2. Sample preparation and system configuration

For the preparation of the nanowell array as a proof of concept, as illustrated in Fig. 1(a), a 30 nm thick SiN film was first deposited on the top surface of a silicon wafer using Low-Pressure Chemical Vapor Deposition (LPCVD). Next, a 60 nm thick Si film was deposited on top of the SiN film by Plasma Enhanced Chemical Vapor Deposition (PECVD), and then a 50 nm SiN film was deposited on the Si layer using LPCVD. Finally, a 60 μm × 60 μm freestanding membrane was obtained by etching the silicon from the backside through a square window using potassium hydroxide (KOH) [36].

The nanowells were defined using electron beam lithography (EBL). After cleaning with acetone and Isopropyl Alcohol (IPA), 200 nm thick Polymethyl Methacrylate (PMMA) photoresist was spun on the sample, then the patterns of the nanowell arrays were written in the PMMA using EBL. After development, Reactive Ion Etching (RIE) with a CHF_3/O_2 flow was used to etch the

Optics EXPRESS

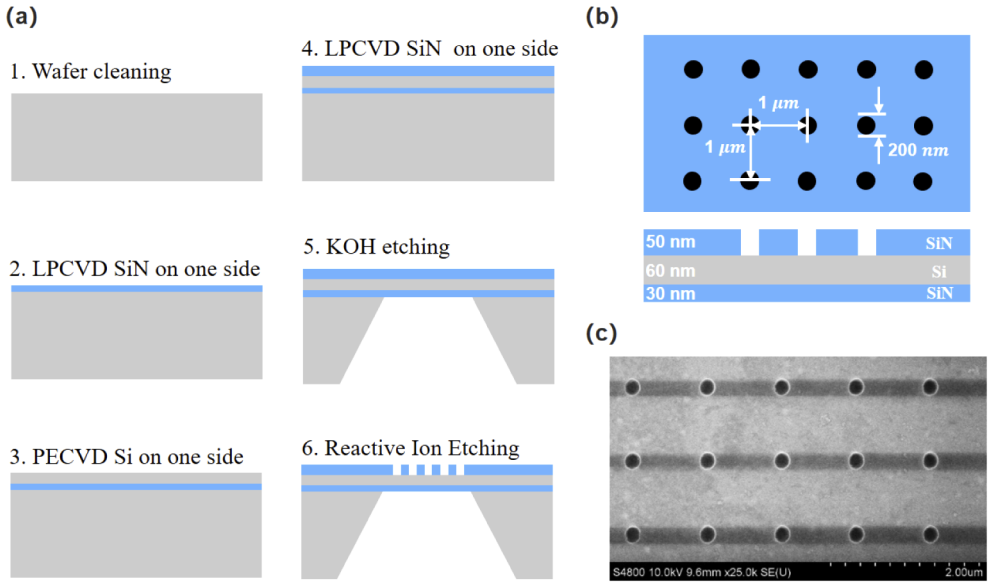

Fig. 1. (a) The fabrication procedure of nanowell array. (b) Schematic and dimensions of the nanowell array. The diameter and depth of the etched nanowells were 200 nm, and 50 nm, respectively. The periodicity of the array was 1 μm. (c) SEM image of the nanowell array.

nanowells into the SiN using the PMMA mask. This dry etch process provides nanowells with vertical and smooth sidewalls. After removing the residual PMMA using acetone, fabrication was completed leaving nanowell arrays with a depth of 50 nm on top of the 60 nm thick Si layer, as schematically shown in Fig. 1(b) and the SEM picture in Fig. 1(c). This structure is designed for efficient capturing and fixation of molecules in the nanowell and enhancement of the optical scattering from the nanowell and trapped molecules.

In the PIMI measurements [37,38], an Olympus reflection microscopic system (BX51M) was used to provide the basic optical path. As illustrated in Fig. 2(a), a Liquid Crystal Polarization Rotator (LCPR) with a modulation angle range of 360° was inserted in the illumination beam path. In the beam path between the objective and the imaging sensor, a quarter-wave plate and a high extinction ratio polarizer were inserted, with fast axes oriented at 45° and 90° with respect to the paper plane, respectively. The imaging sensor was a CCD manufactured by Basler (piA2400-17gm) with a pixel size of 3.45 μm and an output dynamic range of 12 bits. By controlling the LCPR, the polarization angle of the illumination was modulated precisely from 0° through 360° in steps of 18° (as shown in Fig. 2(b)) and the far-field scattering images under each illumination condition were recorded. The intensity variation of the recorded image pixels corresponding to each object point can be formulated as [37,38]:

$$I_i = \frac{1}{2} I_0[1 + \sin\delta \ \sin 2(\theta_i - \phi)] \tag{1}$$

where I_i (the subscript i indicates the number of polarization rotation angles) is the pixel intensity. I_0 represents the average intensity under all polarization states. $\sin\delta$ is the sine of the phase difference between two orthogonal polarization components. θ_i is the polarization angle of the linearly polarized incident beam and ϕ is the polarization ellipse orientation angle of the beam reflected from the sample.

By expanding Eq. (1) trigonometrically, it can be reformulated in the following form:

$$I_i = a_0 + a_1 \sin 2\theta_i + a_2 \cos 2\theta_i. \tag{2}$$

Optics EXPRESS

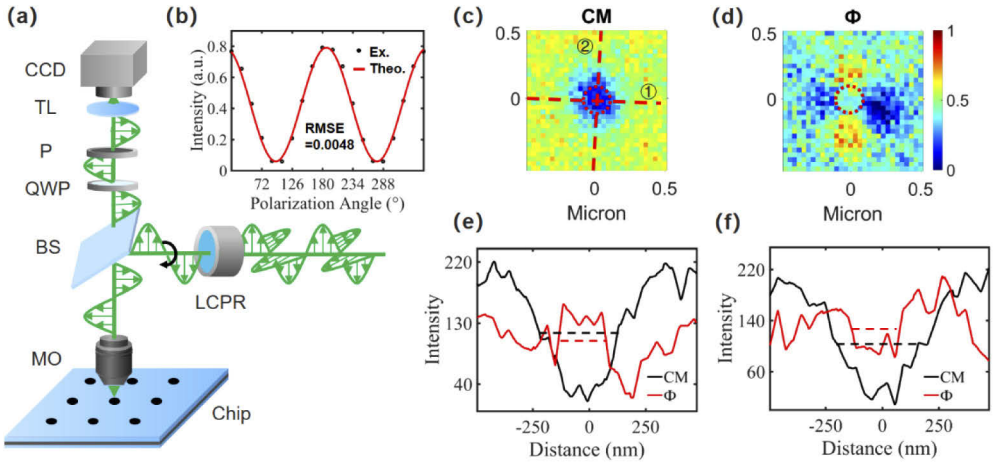

Fig. 2. (a) Schematic configuration of PIMI system, TL: Tube Lens, P: Polarizer, QWP: Quarter Waveplate, BS: Beam Splitter, MO: Microscopic Objective, LCPR: Liquid Crystal Polarization Rotator. (b) The calibration curve of LCPR, the precision of polarization modulation can be up to 99%, Ex.: Experimental data, Theo.: Theoretical curve. (c) & (d) Comparisons of a 200-nm-diameter well imaged by (c) Conventional Microscope (CM) and (d) PIMI method (parameter ϕ). (e) & (f) Comparisons of intensity profiles between CM and ϕ images along dashed lines '①' (e) and '②' (f) in (c). Full Width at Half Maximum (FWHM) of the curves in (e) are 202 nm (parameter ϕ) and 340 nm (CM), respectively; FWHM of the curves in (f) are 209 nm (parameter ϕ) and 369 nm (CM), respectively.

$$a_0 = \frac{1}{2}I_0, \quad a_1 = \frac{1}{2}I_0 \sin\delta cos2\phi, \quad a_2 = -\frac{1}{2}I_0 \sin\delta \sin2\phi. \tag{3}$$

Through precise control of the LCPR, the incident polarization angle θ_i can be modulated from zero to 360 degrees, with a total number of steps N = 360°/18°, and a_0, a_1 and a_2 can be calculated as:

$$a_0 = \sum_{i=1}^{N} \frac{1}{N} I_i, \quad a_1 = \sum_{i=1}^{N} \frac{2}{N} I_i \sin2\theta_i, \quad a_2 = \sum_{i=1}^{N} \frac{2}{N} I_i \cos2\theta_i. \tag{4}$$

Thus, the PIMI parameters I_{dp}, $\sin\delta$ and ϕ can be extracted as shown in Eq. (5) by utilizing the above equations.

$$I_{dp} = a_0, \quad sin\delta = \frac{\sqrt{a_1^2 + a_2^2}}{a_0}, \quad \phi = \frac{1}{2} arccos\left(\frac{a_1}{\sqrt{a_1^2 + a_2^2}}\right). \tag{5}$$

By modulating the polarization state of the incident optical field, PIMI can obtain the photon state spatial distribution spectra generated by the structural characteristics of a nanowell under measurement. Figures 2(c) and 2(d) show comparisons between a conventional microscopic image and a PIMI image of ϕ of a single nanowell. As can be seen, strong scattering distributions around a hole with well-defined edges can be directly seen in the ϕ image, while the CM image only shows a drastically blurred airy disk due to the diffraction limit. Figures 2(e) and 2(f) compare the intensity profiles of CM and PIMI images along the dashed lines '①' and '②' in Fig. 2(c), respectively. The spatial scattering distributions in the PIMI image contain more fine features than those in the CM image. These features are proved to be related to the structural properties of the scatterer, i.e. the well, as demonstrated by the high-resolution images of the nanowells reconstructed with a neural network in section 4 "results and discussions" section

Optics EXPRESS

below. Also, Full Width at Half Maximum (FWHM) as marked with dashed lines in Figs. 2(e) and 2(f) show that the size of features can be obtained with considerably more accuracy from the PIMI image than the CM image.

3. Finite Difference Time Domain method simulation

The Finite Difference Time Domain (FDTD) method was used to simulate the scattering distribution from nanowells in the near field. The FDTD model of the nanowell array is configured as shown in Fig. 1(b). To implement the necessary radiating boundary conditions, the model is sandwiched by periodic boundary conditions. The source is chosen as a plane wave with a wavelength of 532 nm corresponding to the experimental setup. To ensure accurate simulation results, the mesh size is set to 4 nm (length) × 4 nm (width) × 10 nm (height). All the field components have been confirmed to decay to zero when the simulation ended, which means that simulation has run for a sufficiently long time for the Fourier transform to be valid [39].

4. Results and discussions

Simulation of scattering from a single 200-nm-diameter nanowell was performed as shown in Fig. 3(c). As can be seen, there are similar scattering distributions around the nanowell in both the experimental and simulated images. The orientation of the scattering dipoles is also the same. Comparisons of intensity profiles between the PIMI experiment and FDTD simulation along the scattering dipoles are plotted in Figs. 3(b) and 3(d). It is found that the intensity curve changes abruptly at the edges of the nanowell in both the simulated and PIMI results due to the sudden variation of the refractive index. The edge of the nanowell was easily determined from the abrupt variation point of the intensity profile curve of the PIMI result. By taking advantage of the high sensitivity of the polarization status of scattered photons from anisotropically structured material, especially scattering from regions where the sample shows abrupt dimensional and dielectric variations, the PIMI method can easily image morphological variations across samples. We would emphasize that the distributions of the spatial scattering from nanowells depend on the vertical shape of the nanowell and the surface profile at the bottom of the nanowell. Asymmetric distributions of the spatial scattering exist when there is an irregular vertical profile and uneven surface profile at the bottom of the nanowells (details in S1 of Supplement 1). This also explains the asymmetry seen in the PIMI images.

Experiments on nanowell arrays were also carried out. Nanowells with a diameter of 200 nm were fabricated on a square lattice with a period of 1 μm. As illustrated in Fig. 4, different imaging methods were used to characterize the nanowell arrays. Figure 4(a) shows CM results while Fig. 4(d) shows results from an SEM micrograph of a nanowell array. Separated point spread functions which represent nanowells can be found in the CM image, but it is almost impossible to recover the shape and size of the nanowells. Compared with the CM results, the PIMI image ϕ shows considerable improvements in resolving the shape and size of each well in the array through the photon state distributions, as shown in Fig. 4(b). FDTD simulations were also performed as shown in Fig. 4(c). From Figs. 4(b) and 4(c), similarities in the spatial scattering distributions can be seen. In addition, by comparing the intensity profiles along two perpendicular lines (0° and 90°), it can be seen that the variations in the PIMI results exhibit more information related to the structures of the nanowell array than in the CM results. Also, the variations in PIMI and FDTD simulation results as marked with black dashed ellipses in Figs. 4(b) and 4(c) show strong similarities.

Experiments on nanowell arrays were also carried out. Nanowells with a diameter of 200 nm were fabricated on a square lattice with a period of 1 μm. As illustrated in Fig. 4, different imaging methods were used to characterize the nanowell arrays. Figure 4(a) shows conventional microscope (CM) results while Fig. 4(d) shows results from an SEM micrograph of a nanowell array. Separated point spread functions which represent nanowells can be found in the CM image,

Optics EXPRESS

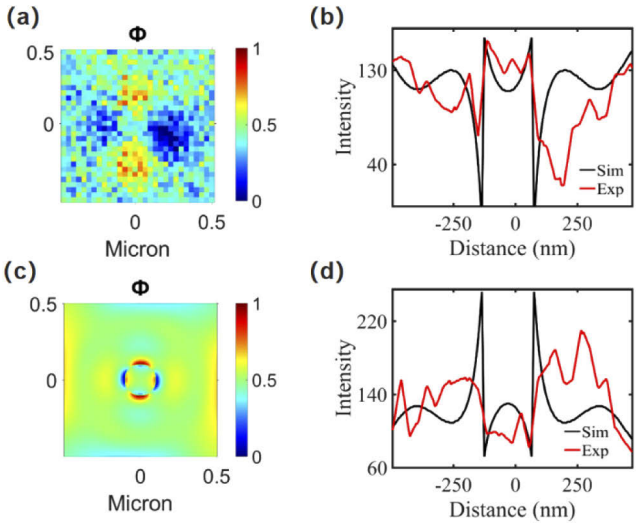

Fig. 3. (a) & (c) Comparisons of the scattering from a 200-nm-diameter nanowell by (a) PIMI method and (c) FDTD simulation. (b) & (d) Comparisons of intensity profiles between PIMI and FDTD images along the same positions as marked with dashed lines '①' (b) and '②' (d) in Fig. 2(c).

but it is almost impossible to recover the shape and size of the nanowells. Compared with the CM results, the PIMI image ϕ shows considerable improvements in resolving the shape and size of each well in the array through the photon state distributions, as shown in Fig. 4(b). FDTD simulations were also performed as shown in Fig. 4(c). From Figs. 4(b) and 4(c), similarities in the spatial scattering distributions can be seen. In addition, by comparing the intensity profiles along two perpendicular lines (0° and 90°), it can be seen that the variations in the PIMI results exhibit more information related to the structures of the nanowell array than in the CM results. Also, the variations in PIMI and FDTD simulation results as marked with black dashed ellipses in Fig. 4(b) and (c) show strong similarities.

Moreover, as plotted in Figs. 4(b) and 4(c), the positions and sizes of nanowells obtained by the PIMI method and FDTD simulation are indicated by the pairs of vertical dashed lines. Comparison of the intensity profiles of the PIMI and FDTD simulation indicates that the edges of the nanowells can be easily determined in the PIMI result. To sum up, by spatially modulating the photon state of the illumination, then filtering and fitting the far-field variation of the scattered photons, PIMI can recover information about the size of subwavelength nanowells, which are almost invisible in the CM image. Here we would highlight the PIMI method has resolution of around 88 nm. Based on our simulations, the smallest nanowell diameter that can be detected by PIMI method is around 50 nm (details in S2 and S3 of Supplement 1).

By taking advantage of the ability of the PIMI method to resolve subwavelength nanostructures, preliminary experiments were conducted for detecting biological molecules trapped in a single nanohole. Two nanoholes with different diameters were imaged using the PIMI method, before and after modification with Shp2 protein (the modification procedure is detailed in S4 of Supplement 1). Shp2 protein is a key molecule in the development of Juvenile Myelomonocytic Leukemia (JMML) cancer [40–42] and being able to sense and characterize the protein is important for understanding the cancer's molecular mechanism. Figures 5(a) and 5(b) show results for an 80-nm-diameter nanohole and Figs. 5(c) and 5(d) for a 109-nm-diameter nanohole. Figures 5(a) and 5(c) show results for empty nanoholes while Figs. 5(b) and 5(d) show results for nanoholes modified with protein. By comparing the scattering spatial distributions of the PIMI

Optics EXPRESS

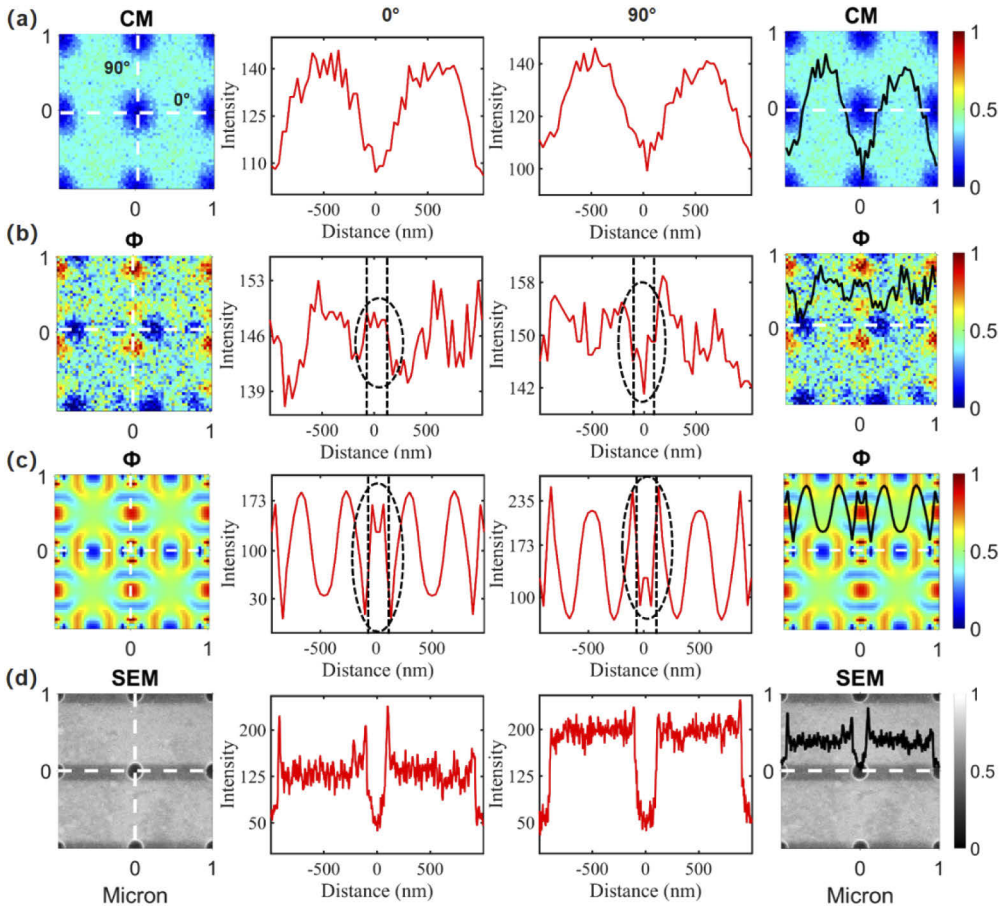

Fig. 4. Comparisons of imaging results on a nanowell array: (a) Conventional Microscope (CM), (b) PIMI method, (c) FDTD simulation and (d) SEM. Intensity profiles across the images along two perpendicular lines (0° and 90°) are plotted. The rightmost row shows images with intensity curves along the 0° direction. The positions of the edges of nanowells imaged by different methods are indicated by the pairs of vertical dashed lines.

results, we can determine the existence of protein nearby or over the nanohole. The scattering distributions from nanoholes modified with protein are quite different from the empty nanoholes. Here we would highlight that the changes of protein volume present in the nanowells can also be distinguished from the spatial scattering distributions. According to the simulations, the sensing volume of the nanowells is at least as small as 2.463 *nl* (details in S5 of Supplement 1). In order to increase the effectiveness of the protein binding protocol, the key challenge is to increase the number of nanowells that are occupied with the Shp2 protein.

Figure 6 shows a preliminary result of applying deep learning in reconstructing the shape of the nanowell array. By choosing the SEM image as the ground truth, the PIMI image (shown in Fig. 6 left) was used as the input to train a deep learning network (details in S6 of Supplement 1). As can be seen, the positions and dimensions of the nanowell array were recovered clearly in the trained image. To make a quantitative comparison, the central nanowell in the ϕ image (in Fig. 6 left) was chosen to calculate the FWHM along the horizontal and vertical directions. Table 1 shows the FWHM measured from the SEM image, the CM image, the ϕ image and the reconstructed image by deep learning. Taking the SEM picture as the reference, the PIMI

Optics EXPRESS

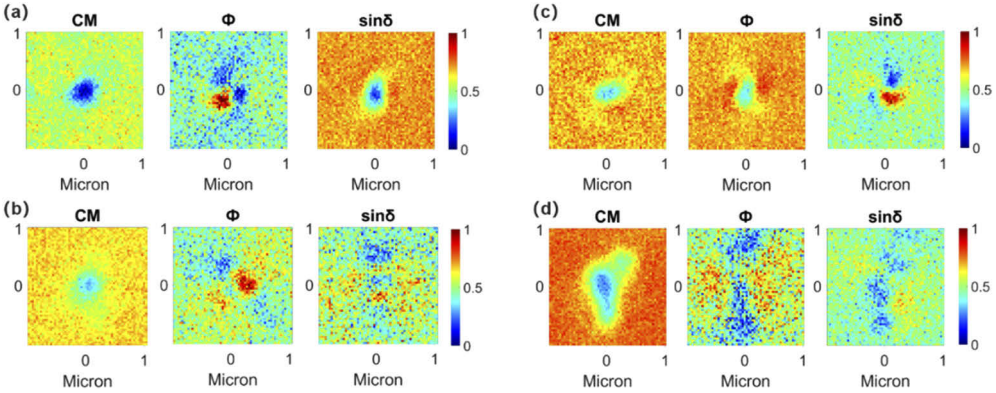

Fig. 5. Comparisons between a single empty nanohole and a nanohole modified with protein Shp2. (a) & (b): an 80-nm-diameter empty nanohole (a) and a nanohole modified with protein Shp2 (b); (c) & (d): an empty 109-nm-diameter nanohole (c) and a nanohole modified with protein Shp2 (d).

technique is significantly more accurate than the CM measurements, reducing the relative errors from 80.4% to 4.0% and 78.6% to 9.7% for the horizontal and vertical directions respectively. The reconstructed image using deep learning is even more accurate, reducing the relative error from 4.0% to 2.5% and 9.7% to 3.4% for the horizontal and vertical directions respectively. Some incomplete nanowells can be observed in the reconstructed image with the left sides of the nanowells appearing weak or having missing parts. The reason for this may be because the left scattering distributions of the PIMI image, used as the input to the deep learning algorithm, are relatively weak. By utilizing PIMI results of nanowells (and also in future nanopores) with different sizes and structures to train a neural network, we believe it will be possible to estimate the position, size and shape of molecules attached to them from the PIMI scattering distributions.

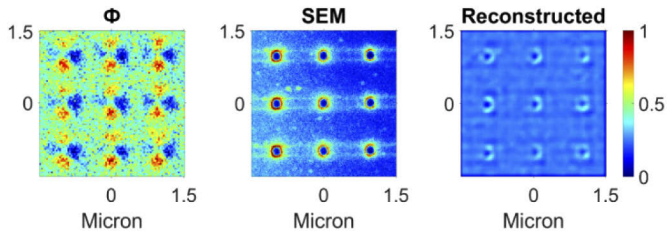

Fig. 6. PIMI image (left), SEM image (middle) and the reconstructed image by deep learning (right).

Table 1. Comparisons of FWHM in different methods.

Method	Horizontal FWHM (nm)	Vertical FWHM (nm)	Horizontal Relative Error (%)	Vertical Relative Error (%)
CM	359	368	80.4	78.6
PIMI	207	226	4.0	9.7
Deep Learning	204	213	2.5	3.4
SEM	199	206	0	0

However, in the current study, the pixel size of the imaging result (i.e., 34.5 nm per pixel) is limited by the magnification of the optical system, which may lead to loss of information due to

Optics EXPRESS

under-sampling in the imaging plane, even if high-resolution scattering spectra were brought to the far-field by the proposed imaging method. To improve the noise performance beyond that of the current system, a scientific CMOS camera with higher quantum efficiency will replace the current CCD camera and a high-speed Electro-Optic Phase Modulator (EOPM) will be used as the polarization modulation module to reduce vibration noise during measurements. In addition, a cross-modality deep-learning method based on a generative adversarial network (GAN) will be utilized to transform the current imaging results to a higher resolution [43], to recover possible lost information in the measured scattering spectra.

5. Conclusions

In conclusion, we have presented a method for imaging the near-field optical scattering distribution of sub-wavelength nanowells on a SiN substrate, by measuring indirect parametric images of the photon state variation in the far field. The strong scattering spatial-spectral signals around nanowells that can be seen in the experimental results were verified by FDTD simulations. These images demonstrated that the photon state bears rich information related to the near-field characteristics of the nanowells and its array arrangements, such as the nanowell size and periodicity. Deep learning techniques further enhance the clarity of the PIMI images. Imaging experiments on a single nanohole modified with Shp2 proteins were also performed. With Shp2 protein, the scattering distribution of a single nanohole displays significant differences compared to that of an empty nanohole. This work highlights the potential possibilities of utilizing nanowells for molecular characterization or in other virus detection applications, by trapping molecules or viral particles to the nanowells and measuring their scattering spatial-spectra in an efficient wide-field manner.

Funding. the National Major Scientific Instruments and Equipment Development Project (Grant No.61827814); National Key Research and Development Program of China (No.2017YFF0107100); Fundamental Research Funds for the Central Universities (30920010011); Natural Science Foundation of Beijing Municipality (Z190018); Engineering and Physical Sciences Research Council (EP/R042578/1); the Ministry of Education collaborative project; Royal Society (Grant IEC/NSFC/181557).

Acknowledgments. This work was supported by the National Major Scientific Instruments and Equipment Development Project under Grant No.61827814, National Key Research and Development Program of China under Grant No.2017YFF0107100), Beijing Natural Science Foundation under Grant No.Z190018, the Fundamental Research Funds for the Central Universities under Grant No.30920010011 and the Ministry of Education collaborative project. They also acknowledge support from the UK Engineering and Physical Sciences Research Council (Grant EP/R042578/1), and from the UK Royal Society (Grant IEC/NSFC/181557).

Disclosures. The authors declare no conflicts of interest.

See Supplement 1 for supporting content.

References

1. T. Gilboa and A. Meller, "Optical sensing and analyte manipulation in solid-state nanopores," Analyst **140**(14), 4733–4747 (2015).
2. D. Branton, D. W. Deamer, A. Marziali, H. Bayley, S. A. Benner, T. Butler, M. D. Ventra, S. Garaj, A. Hibbs, X. Huang, S. B. Jovanovich, P. S. Krstic, S. Lindsay, X. S. Ling, C. H. Mastrangelo, A. Meller, J. S. Oliver, Y. V. Pershin, J. M. Ramsey, R. Riehn, G. V. Soni, V. Tabard-Cossa, M. Wanunu, M. Wiggin, and J. A. Schloss, "The potential and challenges of nanopore sequencing," Nat. Biotechnol. **26**(10), 1146–1153 (2008).
3. J. Clarke, H. Wu, L. Jayasinghe, A. Patel, S. Reid, and H. Bayley, "Continuous base identification for singlemolecule nanopore DNA sequencing," Nat. Nanotechnol. **4**(4), 265–270 (2009).
4. B. M. Venkatesan and R. Bashir, "Nanopore sensors for nucleic acid analysis," Nat. Nanotechnol. **6**(10), 615–624 (2011).
5. E. A. Manrao, I. M. Derrington, A. H. Laszlo, K. W. Langford, M. K. Hopper, N. Gillgren, M. Pavlenok, M. Niederweis, and J. H. Gundlach, "Reading DNA at single-nucleotide resolution with a mutant MspA nanopore and phi29 DNA polymerase," Nat. Biotechnol. **30**(4), 349–353 (2012).
6. M. Ayub, S. W. Hardwick, B. F. Luisi, and H. Bayley, "Nanopore-based identification of individual nucleotides for direct RNA sequencing," Nano Lett. **13**(12), 6144–6150 (2013).
7. B. McNally, A. Singer, Z. Yu, Y. Sun, Z. Weng, and A. Meller, "Optical recognition of converted DNA nucleotides for single-molecule DNA sequencing using nanopore arrays," Nano Lett. **10**(6), 2237–2244 (2010).

Optics EXPRESS

8. G. V. Soni and A. Meller, "Progress toward ultrafast DNA sequencing using solid-state nanopores," Clin. Chem. **53**(11), 1996–2001 (2007).
9. B. M. Venkatesan and R. Bashir, "Solid State Nanopore Sensors for Nucluic Acid Analysis," in *Nanopores, Sensing and Foundamental Biological Interactions* (Springer, 2011).
10. T. Z. Butler, J. H. Gundlach, and M. A. Troll, "Determination of RNA Orientation during Translocation through a Biological Nanopore," Biophys. J. **90**(1), 190–199 (2006).
11. M. Wanunu, S. Bhattacharya, Y. Xie, Y. Tor, A. Aksimentiev, and M. Drndic, "Nanopore analysis of individual RNA/antibiotic complexes," ACS Nano **5**(12), 9345–9353 (2011).
12. M. Wanunu, T. Dadosh, V. Ray, J. Jin, L. McReynolds, and M. Drndić, "Rapid electronic detection of probespecific microRNAs using thin nanopore sensors," Nat. Nanotechnol. **5**(11), 807–814 (2010).
13. C. Plesa, S. W. Kowalczyk, R. Zinsmeester, A. Y. Grosberg, Y. Rabin, and C. Dekker, "Fast translocation of proteins through solid state nanopores," Nano Lett. **13**(2), 658–663 (2013).
14. M. Firnkes, D. Pedone, J. Knezevic, M. Doblinger, and U. Rant, "Electrically facilitated translocations of proteins through silicon nitride nanopores: conjoint and competitive action of diffusion, electrophoresis, and electroosmosis," Nano Lett. **10**(6), 2162–2167 (2010).
15. S. W. Kowalczyk, A. R. Hall, and C. Dekker, "Detection of local protein structures along DNA using solid-state nanopores," Nano Lett. **10**(1), 324–328 (2010).
16. A. Singer, S. Rapireddy, D. H. Ly, and A. Meller, "Electronic barcoding of a viral gene at the single-molecule level," Nano Lett. **12**(3), 1722–1728 (2012).
17. A. Singer, M. Wanunu, W. Morrison, H. Kuhn, M. Frank-Kamenetskii, and A. Meller, "Nanopore based sequence specific detection of duplex DNA for genomic profiling," Nano Lett. **10**(2), 738–742 (2010).
18. J. K. Rosenstein, M. Wanunu, C. A. Merchant, M. Drndic, and K. L. Shepard, "Integrated nanopore sensing platform with sub-microsecond temporal resolution," Nat. Methods **9**(5), 487–492 (2012).
19. F. Traversi, C. Raillon, S. M. Benameur, K. Liu, S. Khlybov, M. Tosun, D. Krasnozhon, A. Kis, and A. Radenovic, "Detecting the translocation of DNA through a nanopore using graphene nanoribbons," Nat. Nanotechnol. **8**(12), 939–945 (2013).
20. G. F. Schneider, S. W. Kowalczyk, V. E. Calado, G. Pandraud, H. Zandbergen, L. M. K. Vandersypen, and C. Dekker, "DNA translocation through graphene nanopores," Nano Lett. **10**(8), 3163–3167 (2010).
21. C. A. Merchant, K. Healy, M. Wanunu, V. Ray, N. Peterman, J. Bartel, M. D. Fischbein, K. E. Venta, Z. Luo, A. T. C. Johnson, and M. Drndić, "DNA translocation through graphene nanopores," Nano Lett. **10**(8), 2915–2921 (2010).
22. S. Garaj, W. Hubbard, A. Reina, J. Kong, D. Branton, and J. A. Golovchenko, "Graphene as a subnanometre trans-electrode membrane," Nature **467**(7312), 190–193 (2010).
23. B. M. Venkatesan, D. Estrada, S. Banerjee, X. Jin, V. E. Dorgan, M. Bae, N. R. Aluru, E. Pop, and R. Bashir, "Stacked graphene-Al2O3 nanopore sensors for sensitive detection of DNA and DNA-protein complexes," ACS Nano **6**(1), 441–450 (2012).
24. D. Axelrod, "Total internal reflection fluorescence microscopy in cell biology," Traffic **2**(11), 764–774 (2001).
25. K. N. Andersen, W. E. Svendsen, T. Stimpel-Lindner, T. Sulima, and H. Baumgärtner, "Annealing and deposition effects of the chemical composition of silicon-rich nitride," Appl. Surf. Sci. **243**(1-4), 401–408 (2005).
26. G. V. Soni, A. Singer, Z. Yu, Y. Sun, B. McNally, and A. Meller, "Synchronous optical and electrical detection of biomolecules traversing through solid-state nanopores," Rev. Sci. Instrum. **81**(1), 014301 (2010).
27. S. Inoué, "Foundations of Confocal Scanned Imaging in Light Microscopy," in *Handbook of Biological Confocal Microscopy* (Springer, 2006).
28. N. Di Fiori, A. Squires, D. Bar, T. Gilboa, T. D. Moustakas, and A. Meller, "Optoelectronic control of surface charge and translocation dynamics in solid-state nanopores," Nat. Nanotechnol. **8**(12), 946–951 (2013).
29. P. Chen, T. Mitsui, D. B. Farmer, J. Golovchenko, R. G. Gordon, and D. Branton, "Atomic Layer Deposition to Fine-Tune the Surface Properties and Diameters of Fabricated Nanopores," Nano Lett. **4**(7), 1333–1337 (2004).
30. H. T. Chorsi, Y. Lee, A. Alù, and J. X. J. Zhang, "Tunable plasmonic substrates with ultrahigh Q -factor resonances," Sci. Rep. **7**(1), 15985 (2017).
31. M. T. Chorsi and H. T. Chorsi, "Graphene plasmonic nanogratings for biomolecular sensing in liquid," Appl. Phys. A **123**(12), 757 (2017).
32. G. P. Wiederrecht, "Near-field optical imaging of noble metal nanoparticles," The European Physical Journal Applied Physics **28**(1), 3–18 (2004).
33. L. Novotny, D. W. Pohl, and P. Regli, "Near-field, far-field and imaging properties of the 2D aperture SNOM," Ultramicroscopy **57**(2-3), 180–188 (1995).
34. V. Sandoghdar and J. Mlynek, "Prospects of apertureless SNOM with active probes," J. Opt. A: Pure Appl. Opt. **1**(4), 523–530 (1999).
35. R. C. Reddick, R. J. Warmack, D. W. Chilcott, S. L. Sharp, and T. L. Ferrell, "Photon scanning tunneling microscopy," Rev. Sci. Instrum. **61**(12), 3669–3677 (1990).
36. L. Liu, H. Wu, Y. Xuan, X. Wang, Y. Zhang, Y. Chen, and Q. Liu, "Study on the Size Shrinking and Shape Changing of Solid-State Nanopores," Adv. Mat. Res. **189-193**, 3218–3221 (2011).
37. X. Liu, B. Qiu, Q. Chen, Z. Ni, and L. Gui, "Characterization of graphene layers using super resolution polarization parameter indirect microscopic imaging," Opt. Express **22**(17), 20446–20456 (2014).

Optics EXPRESS

38. K. Ullah, X. Liu, M. Habib, and Z. Shen, "Subwavelength Far Field Imaging of Nanoparticles with Parametric Indirect Microscopic Imaging," ACS Photonics **5**(4), 1388–1397 (2018).
39. A. Demetriadou, "The impact of natural modes in plasmonic imaging," Sci. Rep. **5**(1), 18247 (2016).
40. L. Dong, H. Zheng, and C. Qu, "CCL3 is a key mediator for the leukemogenic effect of Ptpn11 activating mutations in the stem cell microenvironment," Blood **130**(12), 1471–1474 (2017).
41. L. Dong, W. Yu, H. Zheng, M. L. Loh, S. T. Bunting, M. Pauly, G. Huang, M. Zhou, H. E. Broxmeyer, D. T. Scadden, and C. Qu, "Leukaemogenic effects of Ptpn11 activating mutations in the stem cell microenvironment," Nature **539**(7628), 304–308 (2016).
42. X. Li, L. Dong, W. Xu, S. S. Bhuyan, C. Chen, and R. Wang, "Study of SHP-2 (PTPN11) allosterism on structural movement using solution perturbed molecular dynamics simulation," J. Mol. Liq. **223**, 509–515 (2016).
43. H. Wang, Y. Rivenson, Y. Jin, Z. Wei, R. Gao, H. G. Günaydın, L. A. Bentolila, C. Kural, and A. Ozcan, "Deep learning enables cross-modality super-resolution in fluorescence microscopy," Nat. Methods **16**(1), 103–110 (2019).